3-D Multi-Input Multi-Output (MIMO) Pulsed Chaos Lidar Based on Time-Division Multiplexing

Jun-Da Chen, Kuan-Wei Wu, Hsin-Lin Ho, Cheng-Ting Lee, and Fan-Yi Lin, *Member, IEEE*

***Abstract*—In this study, we propose and evaluate a 3D multi-input multi-output (MIMO) pulsed chaos lidar based on time-division multiplexing. By time-gating a chaos waveform sequentially at different times, chaos-modulated pulses for different channels that are uncorrelated with each other can be generated. To quantitatively evaluate the anti-interference/jamming capability, we investigated the detection performance of the MIMO chaos lidar under different jamming strengths and overlapped ratios between the jamming and the signal pulses. The overall detection probabilities of the chaos lidar and a conventional time-digital-converter-based pulsed lidar under the influence of interference/jamming were compared and we found that the chaos lidar exhibits strong resistance to the interference/jamming. Employing the 3D MIMO chaos lidar developed, we demonstrate 3D imaging under the influence of interference/jamming. By simultaneously scanning 2 different channels with overlapped field-of-views (FOVs), 3D images with large-FOV/low-resolution and small-FOV/high-resolution were obtained at the same time.**

***Index Terms*—Semiconductor lasers, chaos, laser Radar, jamming, interference suppression, optical feedback, MIMO system.**

I. Introduction

LIDAR has the unique advantage of providing high-accuracy depth information up to a very long detection range. In recent years, 3D lidars have been widely used in applications such as autonomous vehicles, augmented reality/virtual reality, industrial automation, and simultaneous localization and mapping [1]–[4]. Conventional pulsed lidars use repeated optical pulses as the light source. They measure the time-of-flight of the pulses reflected from the target to obtain depth information [5], [6]. Although the concept is simple, using pulses without any specific patterns makes these lidars vulnerable to interference and malicious jamming [7]. To mitigate these issues, correlation-based lidars such as random-modulation continuous-wave (RM-CW) lidars [8]–[10] and chaos lidars [11]–[14] that utilize modulated light with specific patterns have been proposed.

Manuscript received December 11, 2021; revised January 31, 2022; accepted February 8, 2022. Date of publication February 14, 2022; date of current version March 9, 2022. This work was supported in part by the Ministry of Science and Technology, Taiwan (MOST) under Grant 110-2218-E-007-047, and in part by the National Tsing Hua University under Grants 110QI039E1 and 110Q2715E1. *(Corresponding author: Fan-Yi Lin.)*

The authors are with the Department of Electrical Engineering and Institute of Photonics Technologies, National Tsing Hua University, Hsinchu 300, Taiwan (e-mail: mmmevery@gmail.com; webb12197@gmail.com; a0972305396@gmail.com; c2811608@gmail.com; fylin@ee.nthu.edu.tw).

Color versions of one or more figures in this article are available at https://doi.org/10.1109/JSTQE.2022.3150791.

Digital Object Identifier 10.1109/JSTQE.2022.3150791

An RM-CW lidar emits light modulated with pseudo-random binary sequences. By calculating the cross-correlation between the transmitted and received sequences, the range of the target can be determined. Although RM-CW lidars can mitigate the influence of interference and jamming, high-speed optoelectronics are required to generate and modulate the codes.

Without the need for high-speed modulators and electronics for pattern generation and modulation, CW chaos lidars generate chaos-modulated light by utilizing intrinsic laser dynamics. [15]–[19]. They have no range ambiguity and are intrinsically resistant to interference and jamming because of their noise-like waveforms.

Despite these unique features, the correlation-based lidars with modulated CW waveforms typically have relatively low signal-to-noise ratios (*SNRs*) especially when the output power is limited by eye-safe regulations (average power less than 10 mW at 1550 nm) [20]–[23]. Although it is possible to increase the *SNR* by increasing the accumulation time window of detection, the detection throughput will be limited making them not suitable for real-time high-speed 3D imaging that requires fast detection with high throughput.

To take advantage of both the pulsed and modulated CW lidars, we proposed and studied a 3D pulsed chaos lidar system that utilizes chaos-modulated pulses to improve the *SNR* [24]–[27]. By employing a pulsed master oscillation power amplifier (MOPA) scheme and quadrant avalanche photodetectors (APDs) [28], [29], high-speed 3D imaging at a throughput of 100 kHz, a frame rate of 10 Hz, and a field-of-view (FOV) of 24.5 $\times$ 11.5 degrees have been demonstrated. While the detection performance of the single-input single-output (SISO) chaos lidar system keeps being improved, its FOV is still limited by the mechanical turning angle of the micro-electro-mechanical system (MEMS) mirror and the physical parameters of the receiving optics. Moreover, the throughput and precision are also limited by the peak power and the energy of the generated pulses.

To increase the FOV and the throughput, multiple SISO lidars can be integrated into a multi-channel lidar [30], [31]. In conventional pulsed lidars, to avoid interference between channels, the FOV of each adjacent channel must be limited to reduce the overlapped region and the pulses of each channel must be emitted in sequence outside other's detection time windows to avoid ambiguity. When integrating with chaos lidars, the interference between the channels can be significantly mitigated.

In this study, we developed a MIMO 3D pulsed chaos lidar based on time-division multiplexing. By time-gating a CW chaos

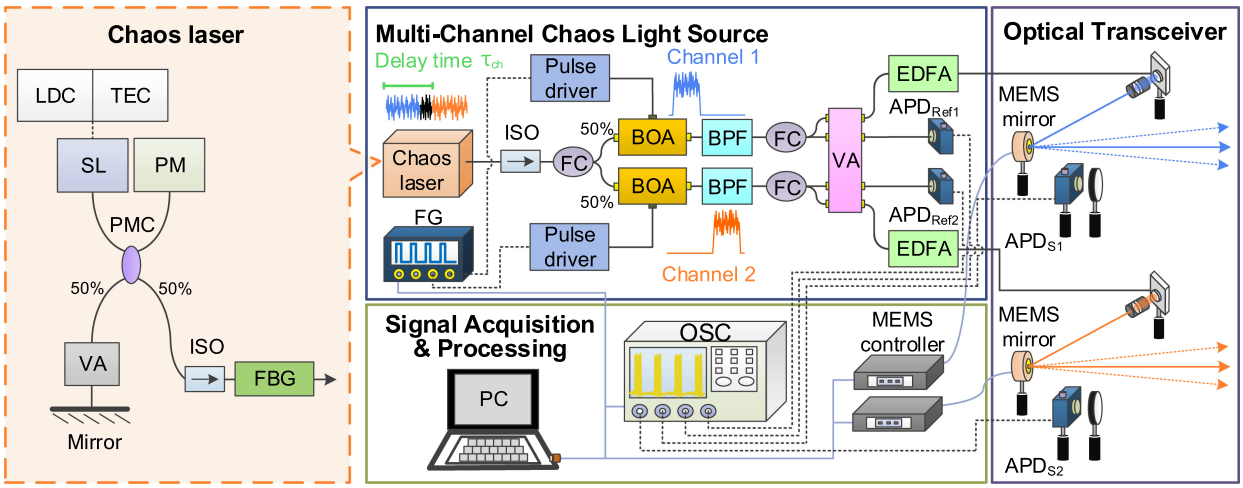

Fig. 1. Schematic of a MIMO 3D pulsed chaos lidar based on time-division multiplexing. LDC: laser diode controller; TEC: temperature controller; SL: semiconductor laser; PMC: polarization-maintaining fiber coupler; VA: variable optical attenuator; PM: power meter; ISO: isolator; FGB: fiber Bragg grating; BOA: booster optical amplifier; BPF: band-pass filter; FG: function generator; FC: fiber coupler; EDFA: Erbium-doped fiber amplifier; APD: avalanche photodetector; OSC: oscilloscope; PC: personal computer.

waveform at different times, we can generate multiple channels of chaos-modulated pulses with low correlation to each other. We investigated the correlation property of the pulses generated under different relative delay times τ_{ch} and pulsewidths PW. We evaluated the peak to standard deviation of sidelobe level (PSL_{std}), precision, and detection probability of the lidar under different relative jamming strengths and overlapped ratios to quantify its anti-interference/jamming capability. We compared the chaos lidar with the time-to-digital converter (TDC) based lidars and quantitatively evaluated their overall detection probability. For demonstration, we present 3D imaging under malicious jamming and demonstrate multi-channel 3D imaging with simultaneous large-FOV/low-resolution and small-FOV/high-resolution scanning.

II. Experimental Setup

Fig. 1 presents a schematic of a MIMO 3D pulsed chaos lidar based on time-division multiplexing (TDM). The system mainly comprises a multi-channel chaos light source, an optical transceiver, and a signal acquisition and processing module.

In the multi-channel chaos light source module, we use a 1550-nm single-mode semiconductor laser (Shengshi Optical SWLD-155005P8-FC/APC-PM) subject to optical feedback from a fiber mirror as the chaos laser. With a feedback strength ξ_{fb} (defined as the ratio between the reflected and emitted optical fields) of 0.017 and a feedback time delay τ_{fb} of 65 ns controlled by the variable optical attenuator (VA) and the fiber length, the laser outputs CW chaos that has a broadened spectrum. We used a power meter (PM) to monitor ξ_{fb} and an isolator (ISO) to avoid any unwanted feedback. To better match with the detector bandwidth, we used a fiber Bragg grating (FGB; IXblue IXC-FBG-PS-1550-1-ATH-PM-C, linewidth $<$1 GHz) to reduce the linewidths of the chaos waveforms and thus enhance the modulation depth for better detection capability [29].

To generate multi-channel chaos-modulated pulses, we can divide the laser output into the number of channels needed with fiber couplers. For this experiment, we used a 50:50 fiber coupler to split the CW chaos into two channels and then send them into the corresponding booster optical amplifiers (BOA, Thorlabs BOA1130P) for pulse generation. By adjusting the relative onset delay times between the two pulse drivers (AeroDIODE, CCS-std) with the function generator (FG; Agilent 81150 A), we generated uncorrelated chaos-modulated pulses with the modulations time-gated from different parts of the CW chaos waveform. We then sent these pulses into the band-pass filters (BPF; Fiber Optic M-AD-1) to reduce the amplified spontaneous emissions from the BOAs and use two erbium-doped fiber amplifiers (EDFAs) (Channel 1: GIP CGBC1E3128001 A; Channel 2: GIP EFAS1EB128002 A) to amplify them in a pulsed MOPA configuration [28]. To record the waveforms of these two input pulses with channel 1 and channel 2 as the references, we used fiber couplers before the EDFAs to split the lights and detect them with two identical avalanche photodetectors (APD; Thorlabs APD430 C, 400 MHz). Here the input pulses of channel 1 and channel 2 arrive at the respective $\mathrm{APD_{Ref1}}$ and $\mathrm{APD_{Ref2}}$ sequentially with a relative channel delay time τ_{ch} set by the FG. A multi-channel variable optical attenuator was also used to adjust the optical power in each optical path.

In the optical transceiver module, we used a two-axis MEMS mirror (Mirrorcle S6249) in each channel to scan the light emitted from the chaos light source. In channel 1 and channel 2, we used $\mathrm{APD_{S1}}$ and $\mathrm{APD_{S2}}$, respectively, identical to those used for the references to detect the output pulses from the backscattered light as the signals.

In the signal acquisition and processing module, we used an oscilloscope (Tektronix MSO58) to simultaneously acquire the waveforms of the reference and signal at a sampling rate of 1.25 GHz. To measure the range of a target, we first used the second-order Chebyshev high-pass digital filter with a cutoff frequency of 1 MHz to remove the square-wave modulation in the waveforms that define the widths of the pulses. By calculating the lag time of the cross-correlation peak between the input pulse from the reference and the output pulse from

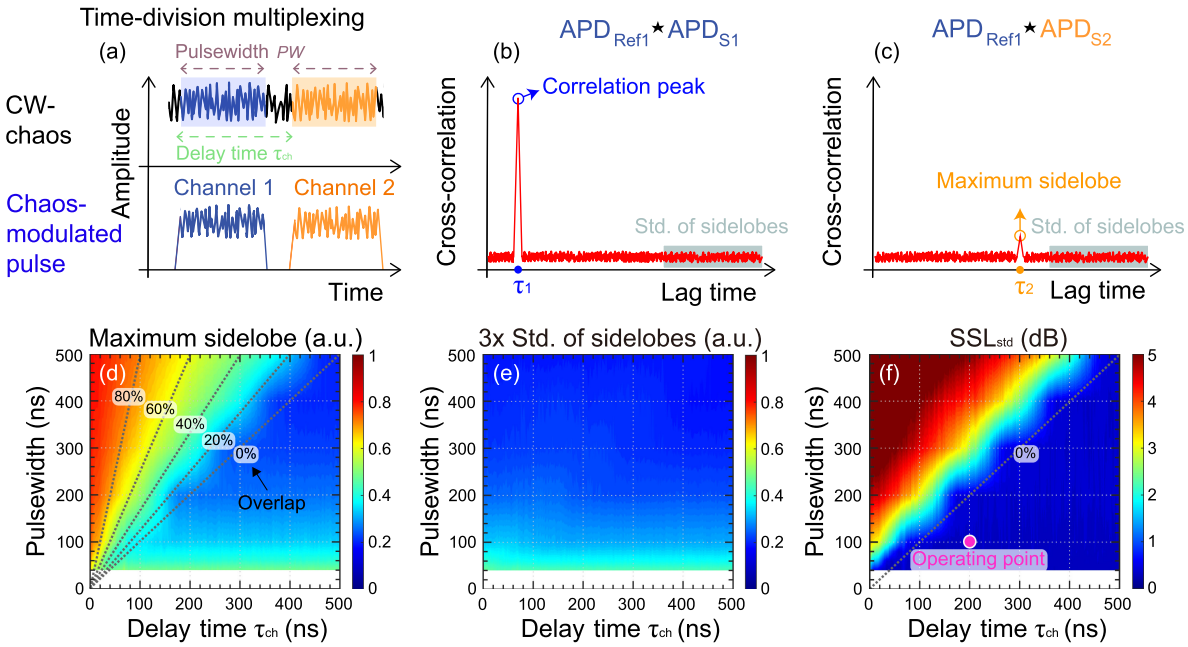

Fig. 2. (a) Schematic illustration of multi-channel chaos-modulated pulses generated by time-division multiplexing. (b) Cross-correlation between the reference and signal pulses of channel 1. (c) Cross-correlation between the reference pulse of channel 1 and the signal pulse of channel 2. (d) Maximum sidelobe, (e) 3 times the standard deviation of sidelobes, and (f) SSL_{std} under different *PW* and τ_{ch}.

the signal with a personal computer, the range of the target can be determined. While some time-delay signatures (TDS) could exist in the cross-correlation trace inherited from the nature of the feedback scheme, we found that they hardly have any influence in lidar applications since only the strongest peak is being recorded. Not to mention that the TDS can always be effectively mitigated or shifted out of the detection window by optimizing the operational parameters or the feedback schemes [19], [32], [33]. In searching for the peak, we incorporated the Spline interpolation [34] to achieve better precision in this study. To automatically and continuously acquire ranges to render 3D images, the FG sends trigger signals to synchronize the pulse drivers, the MEMS mirrors, and the signal acquisitions in each module.

III. Characteristics of Multi-Channel Chaos

To prevent interference between channels, the operation condition to generate input pulses with minimized cross-correlation must be first characterized. As presented in Fig. 2, we investigated the correlation properties of the input pulses generated with different *PW* and τ_{ch} between the channels. Fig. 2(a) illustrates the schematic of multi-channel chaos generated by the TDM. By time-gating different parts of the CW chaos that have uncorrelated oscillation waveforms, chaos-modulated pulses differing from one another can be generated. While multiple uncorrelated pulses can be generated in sequence to be used for several channels, we only demonstrate the case with 2 pulses for simplicity. For channel 1, the pulses from channel 2 can be viewed as the interference (or jamming).

Figs. 2(b) and 2(c) illustrate the cross-correlations between the signal pulse and the reference pulse of channel 1 and the signal pulse of channel 2 and the reference pulse of channel 1, respectively. The values of the correlation peak and the maximum sidelobe exhibit how similar they are and the lag times of τ_1 and τ_2 indicate the relative delays between them. We calculated the PSL_{std} (the value of correlation peak to 3 times the standard deviation of the sidelobes level) to evaluate the detection capability and the SSL_{std} (the value of maximum sidelobe to 3 times the standard deviation of the sidelobes level) to quantify the robustness against interference/jamming.

Figs. 2(d)–(f) present the maximum sidelobe, 3 times the standard deviation of the sidelobes, and the SSL_{std} obtained from the cross-correlations between the signal pulse of channel 2 and the reference pulse of channel 1 under different τ_{ch} and *PW*. Here the pulse repetition frequency is 100 kHz, the correlation length is the same as the pulsewidth and the average output power of both channels from the EDFA is 10 dBm. As presented in Fig. 2(d), when $\tau_{\mathrm{ch}} = 0$ (no time separation when time-gating the two pulses), the cross-correlations between the pulses from the two channels are over 0.8 (1 means that the pulses in the two channels are completely identical) for different *PW*, where the discrepancy between the pulses is mainly because of the noises from the EDFAs and the APDs. As τ_{ch} increases from 0 to the diagonal when $\tau_{\mathrm{ch}} = PW$ (0% overlap between the two pulses), the similarity of the two pulses decreases, and the correlation descends to a level of approximately 0.2. For $\tau_{\mathrm{ch}} \geq PW$, the two pulses are completely separated without any overlapping and the two channels do not effectively interfere with each other. Note that the correlation increases again when the *PW* is shorter than about 80 ns even when the two pulses have 0% overlap. It is due to the shorter correlation lengths that are associated with the shorter pulsewidths [14].

As can be seen in Fig. 2(e), 3 times the standard deviations of the sidelobes are mostly below 0.2 for different τ_{ch} and *PW*. For *PW* shorter than about 80 ns, similar to that shown in Fig. 2(d),

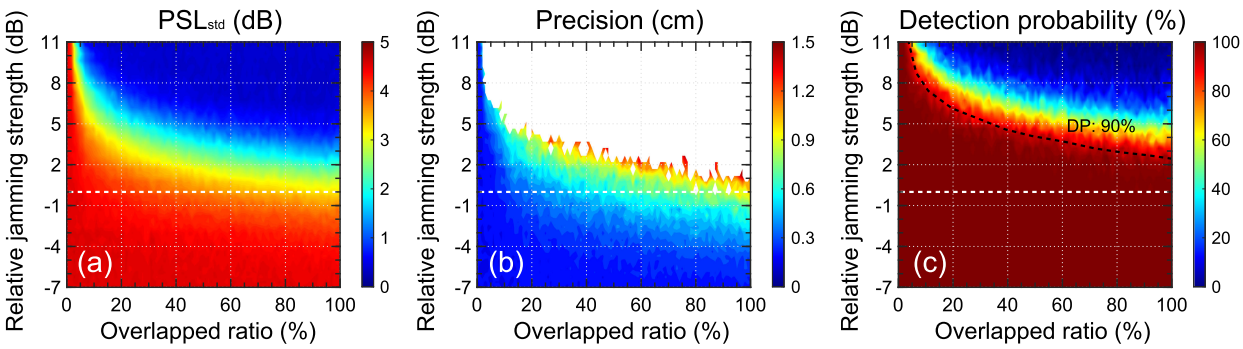

Fig. 3. (a) PSL_{std}, (b) precision, and (c) detection probability under different relative jamming strengths and overlapped ratios. The white dashed lines indicate a relative jamming strength of 0 dB. The black dashed curve in (c) indicates the boundary where the detection probability is 90%.

the value slightly increases to approximately 0.4 because of the shorter correlation lengths.

As illustrated in Fig. 2(f), the SSL_{std} (showing the ratio between Figs. 2(d) and 2(e)) is mostly 0 dB below the diagonal (0% overlap) when $\tau_{\mathrm{ch}} \geq PW$. From the obtained results, we know that by time-gating the pulses with a relative channel delay time of $\tau_{\mathrm{ch}} \geq PW$, interference between the channels can be minimized. For the following assessment and demonstration, we generate pulses with *PW* of 100 ns for a better range precision [28] and τ_{ch} of 200 ns (100 ns time separation between pulses) between channel 1 and channel 2 for minimal interference.

IV. Detection Performance Under Interference and Jamming

To quantify the detection performance under the influence of interference and jamming, Figs. 3(a)–3(c) show the PSL_{std}, precision, and detection probability of one of the channels in the MIMO chaos lidar for different relative jamming strengths and overlapped ratios. Here the pulses from channel 1 are considered as the main signal and the pulses from channel 2 received by channel 1 at $\mathrm{APD_{S1}}$ are viewed as interference or jamming. The relative jamming strength is the ratio between the *SNR* of the jamming signal to the *SNR* of the main signal. The overlapped ratio is the portion of the main signal pulse that is overlapped with the jamming pulse in time. We set the *SNR* of the main signal to 8 dB and varied the *SNR* of the jamming signal from 1 to 19 dB to obtain a relative jamming strength of -7 to 11 dB. The maximum jamming strength examined here is limited by the saturation power of the APDs used. To precisely vary the overlapped ratio continuously, we captured the jamming pulses of different strengths separately and then reproduced them with the main signal pulses with different overlapped ratios through digital signal processing. We have verified that these results are similar to those if the jamming pulses were actually overlapped with the main signal pulses. In Fig. 6, we present a demonstration of when the jamming and signal pulses are received by the $\mathrm{APD_{S1}}$ at the same time with actual overlapping.

As demonstrated in Fig. 3(a), with or without overlapping, the PSL_{std} exceeds 4 dB when the relative jamming strength is small. When there is no overlap (overlapped ratio of 0), the PSL_{std} can be maintained at a high level; greater than 4.5 dB even when the relative jamming strength reaches as strong as 11 dB. In contrast to a conventional TDC-based pulsed lidar that typically fails to detect when the relative jamming strength is above 0 dB, the chaos lidar clearly exhibits its advantages in anti-interference and anti-jamming. Even for the most extreme case when the interference/jamming pulse is completely overlapped with the signal pulse (overlapped ratio of 100%), the PSL_{std} can still be maintained above 3 dB for a relative jamming strength of 0 dB (indicated by the white dashed line).

By taking the standard deviation from 100 measurements, Fig. 3(b) illustrates the precision of ranging under different relative jamming strengths and overlapped ratios. While the precision is governed by both the *SNR* and the bandwidth of the signal [35], [36], the precision indicates the same trend as that of the corresponding PSL_{std}. As can be seen, when there is no overlapping, the precision of the chaos lidar can be maintained at a very low value of 0.18 cm even when the relative jamming strength is as high as 11 dB. For the extreme case of 100% overlapping, the precision is still under 1.03 cm for a relative jamming strength of 0 dB (indicated by the white dashed line). Compared to some commercial 3D pulsed lidars with precisions in the range of several centimeters [24], [30], [31], the chaos lidar possessed a better precision even when under the influence of interference or jamming.

To evaluate the probability of a valid detection, in Fig. 3(c) we plot the detection probability of the chaos lidar under different relative jamming strengths and overlapped ratios. The valid detections account for those detections that have a range error of less than half of the sampling size. In this study, the sampling size is 12 cm associated with the sampling rate of 1.25 GHz. As can be seen, when the overlapped ratio is 0, the detection probability is maintained at 100% (the reddish region) even when the relative jamming strength is as high as 11 dB. While the detection probability gradually decreases as the overlapped ratio or the relative jamming strength increases, for an overlapped ratio of 100%, the detection probability can still hold at 100% for a relative jamming strength of 0 dB. The boundary of the highest jamming strength for the detection probability to be maintained higher than 90% is also plotted (black dashed curve).

From these results, we present that the MIMO chaos lidar is robust to interference and jamming. Although only the results of one of the channels (channel 1) in the MIMO chaos lidar under the influence of interference/jamming (from channel 2) is shown

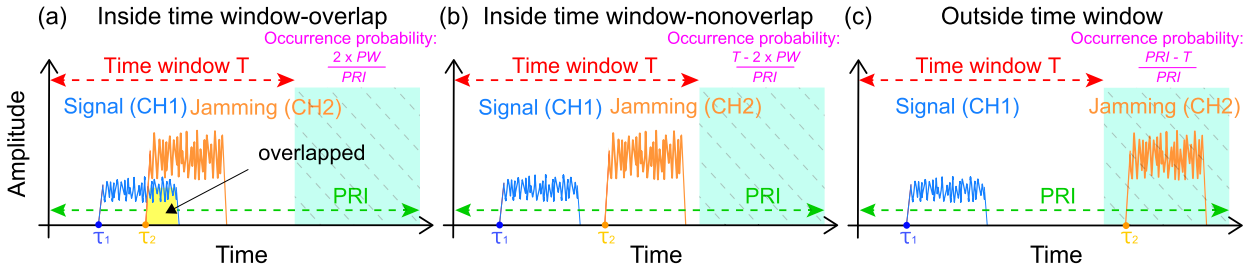

Fig. 4. Three possible scenarios of jamming: the jamming pulse arrives (a) inside the detection time window and has overlapped with the signal pulse either partially or completely, (b) inside the detection time window without overlapping with the signal pulse, and (c) outside the detection time window, respectively.

to prove the concept, the system can easily be expanded into a MIMO lidar with more channels without interfering with each other and yet be robust to jamming.

V. Overall Detection Probability

While we have discussed the detection probability when the jamming (or similarly the interference) pulse is overlapped with the signal pulse, the occurrence probability (*OP*) of the jamming pulse to overlap with the signal pulse in a practical scenario should also be taken into consideration.

Figs. 4(a)–4(c) present the three possible scenarios of jamming: the jamming pulse arrives (a) inside the detection time window and has overlapped with the signal pulse either partially or completely, (b) inside the detection time window without overlapping with the signal pulse, and (c) outside the detection time window. Here we use the signal pulse from channel 1 as the main signal and the pulse from channel 2 as the jamming signal. τ_1 and τ_2 are the lag times of the main signal pulse from channel 1 and the jamming pulse from channel 2 received by the same APD $_{S1}$; *PRI* is the pulse repetition interval; Time window *T* is the receiving time window of the detector for signal processing, which also determines the maximum detection range of the system. The *OP*s of these 3 scenarios can therefore be expressed as *(2 × PW)/PRI*, *(T-2 × PW)/PRI*, and *(PRI-T)/PRI*, respectively. Since the *PW* in a pulsed lidar is usually much shorter than the *PRI* to gain a higher peak power for a better *SNR*, the *OP* for the pulses that have overlapped is typically low as illustrated in Fig. 4(a).

Figs. 5(a) and 5(b) present the detection probability of the chaos lidar and the TDC-based pulsed lidar when the jamming pulse arrives at the detector at a different τ_2. Here we use $\tau_1 = 2.5$ μs, $T = 5$ μs, $PRI = 10$ μs, $PW = 100$ ns, and a relative jamming strength of 3 dB as an example.

As can be seen in Fig. 5(a), for τ_2 between 2.4 to 2.6 μs, the jamming pulse overlaps with the signal pulse. The detection probability of the chaos lidar (blue circles) drops from 100% with minimal overlap to the lowest value of approximately 80% when the jamming pulse overlaps with the signal pulse completely when $\tau_2 = \tau_1 = 2.5$ μs. As for the TDC-based lidar, when the jamming pulse is considered stronger than the signal pulse, no valid detection can be made (i.e. detection probability is 0) other than when $\tau_2 = \tau_1$. In fact, for $\tau_2 = \tau_1$, false detection of the jamming pulse at τ_2 just happens to be at the same position as the signal pulse at τ_1.

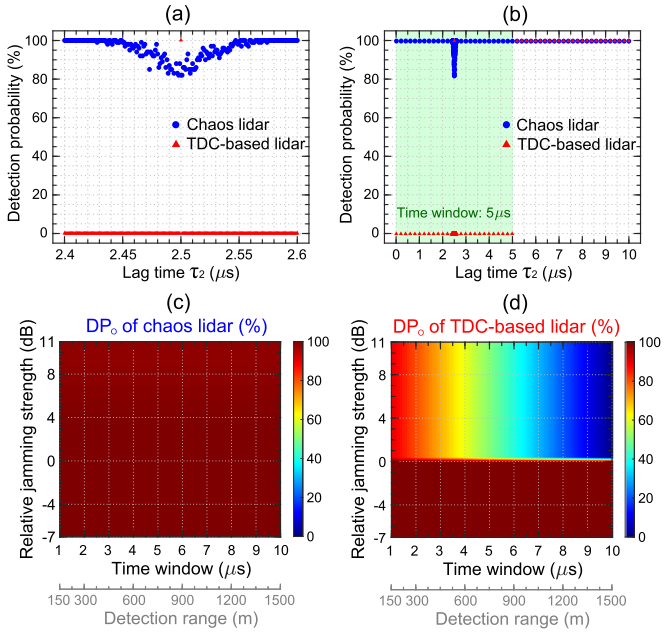

Fig. 5. (a)(b) Detection probability of the chaos and TDC-based lidars when the jamming pulse has a lag time of τ_2. Here we use $\tau_1 = 2.5$ μs, $T = 5$ μs, $PRI = 10$ μs, $PW = 100$ ns, and a relative jamming strength of 3 dB as an example. (a) is a zoomed-in view of (b) at the vicinity of $\tau_1 = 2.5$ μs. (c)(d) DP_o of chaos and TDC-based lidars at different relative jamming strengths and time windows, respectively.

For the entire span of a *PRI*, as presented in Fig. 5(b), the chaos lidar has a detection probability of 100% except in the vicinity around $\tau_2 = 2.5$ μs as discussed in Fig. 5(a). As for the TDC-based lidar, valid detection can only be made when the jamming pulse is outside of the detection time window.

To account for both the detection probability and the occurrence probability, we evaluate the overall detection probability (DP_o) of these lidars:

$$DP_o \equiv \sum_{\tau_2=0}^{PRI} DP(\tau_1, \tau_2) \times OP(\tau_1, \tau_2),$$

where DP_o is the sum of the *DP* multiplied by the *OP* for different τ_2. Here we assumed that τ_1 is within the detection time window and τ_2 is randomly positioned in the *PRI*. While the respective DP_o of the chaos lidar and the TDC-based lidar are 98% and 50% for the cases presented in Figs. 5(a) and 5(b), respectively, we plot more comprehensive mappings of their

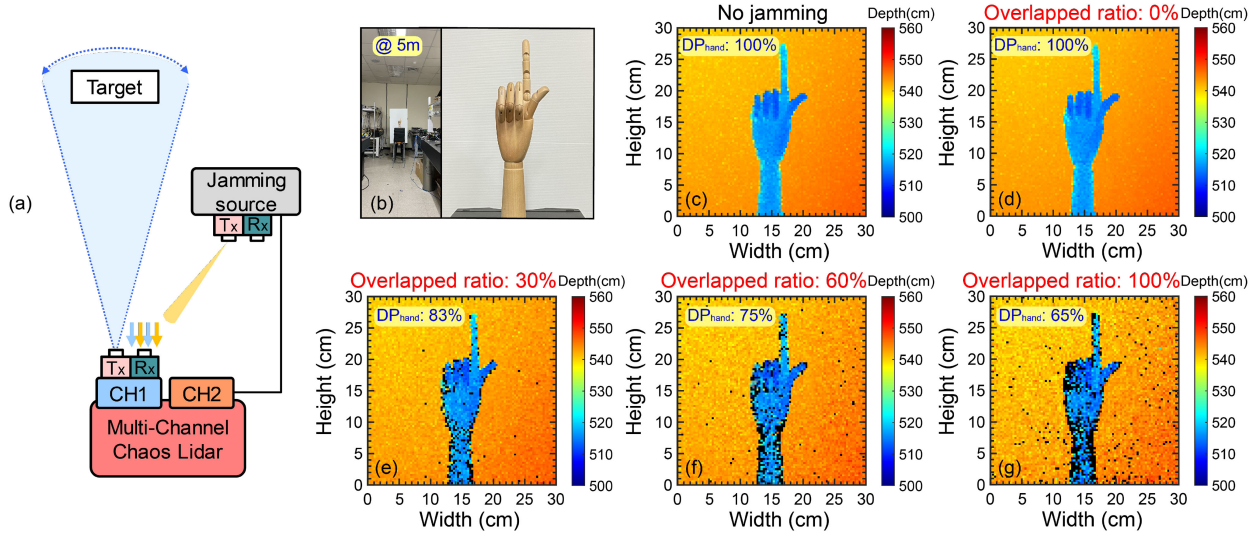

Fig. 6. (a) Illustration of a scenario where one of the channels in the MIMO chaos lidar is interfered with or jammed. Here channel 1 is viewed as the main signal and channel 2 is considered as the interference or jamming source. (b) Photograph of a wooden hand and its 3D rendering obtained using the acquired point cloud (c) without jamming, and jammed with overlapped ratios of (d) 0%, (e) 30%, (f) 60%, and (g) 100%, respectively. $DP_{\rm hand}$ is the detection probability accounting for the ratio of pixels that have valid detection of the hand.

$DP_{\rm o}$ in Figs. 5(c) and 5(d) for the cases with different relative jamming strengths and detection time windows.

Fig. 5(c) depicts the $DP_{\rm o}$ of the chaos lidar under different relative jamming strengths and time windows. As can be seen, when considering both the DP and the OP, the $DP_{\rm o}$ is maintained at a very high level above 98% even when the relative jamming strength is 11 dB, which is much stronger than the signal. By contrast, as presented in Fig. 5(d) for the $DP_{\rm o}$ of the TDC-based lidar, the $DP_{\rm o}$ drops significantly when the detection encounters jamming that is stronger than the signal. Unlike the chaos lidar that can tolerate a significant amount of jamming benefited by the specific chaos-modulated waveforms used, the TDC-based lidar can escape from the influence of jamming only when the jamming pulse happens to arrive at a time outside of the detection time window. Therefore, as can be seen in Fig. 5(d), for a relative jamming strength above 0 dB, the $DP_{\rm o}$ decreases as the time window T increases. When $T = PRI = 10\ \mu$s for a corresponding maximum detection range of 1500 m, the $DP_{\rm o}$ of the TDC-based lidar is essentially 0. While different system operation parameters tailored to different applications and scenarios can be used, in general, we show that the $DP_{\rm o}$ of the chaos lidar is much higher than the TDC-based lidar when experiencing strong jamming or equivalent interference.

VI. Demonstration of 3D Imaging Under the Influence of Interference or Malicious Jamming

In Fig. 6, we demonstrate 3D imaging under the influence of interference and malicious jamming with different overlapped ratios. Fig. 6(a) depicts a scenario of the chaos lidar where the detection of channel 1 is being constantly interfered by channel 2. Here channel 2 can be viewed as an interference or malicious jamming emitting similar waveforms. As can be seen in Fig. 6(b), we placed a wooden hand 5 m away from the lidar as the target. We set the average output power of channel 1 (main signal) to 10 mW which resulted in the received signal having an average *SNR* of 9 dB at the center area of the target and 4 dB at the edge of the hand. To ensure a very strong interference or jamming, we adjusted the output power of channel 2 so that the *SNR* of the received signal from channel 2 (considered as the interference or jamming signal) is 10 dB, which is stronger than the main signal across the whole scanning region. With a relative jamming strength between 1 to 6 dB, false detections are expected in a TDC-based lidar if the jamming pulses happen to arrive within the detection time window.

Fig. 6(c) presents the 3D rendering of the wooden hand obtained using the acquired point cloud without jamming. The image has a resolution of 100×100 pixels taken at a $PRI = 10\ \mu$s (detection throughput or pixel rate of 100 kHz). The profile of the hand and the details of the fingers are clearly depicted. In this image, all pixels on the hand have a valid detection where the range errors are all less than half of the sampling resolution in depth. As the result, the detection probability accounting for those pixels on the hand $DP_{\rm hand}$ is 100%.

Figs. 6(d)–6(g) present the 3D rendering of the wooden hand obtained by using the acquired point cloud with jamming pulses when the main signal and the jamming pulses are 0%, 30%, 60%, and 100% overlapped in time. The corresponding $DP_{\rm hand}$ are 100%, 83%, 75%, and 65%, where the black dots in the plots indicate the pixels without valid detection. As can be seen, $DP_{\rm hand}$ of 100% is achieved when the signal and the jamming pulses are not overlapped even under such strong jamming. As the overlapped ratio increases, the detection on the edge of the target is prone to fail because of the lower *SNR* of the main signal. Nevertheless, even under the most extreme case of an overlapped ratio of 100% (meaning that at every scanning pixel, the jamming pulses all arrive exactly at the same time as the main signal pulses), the contour of the hand is still observed and the $DP_{\rm hand}$ is kept higher than 65%.

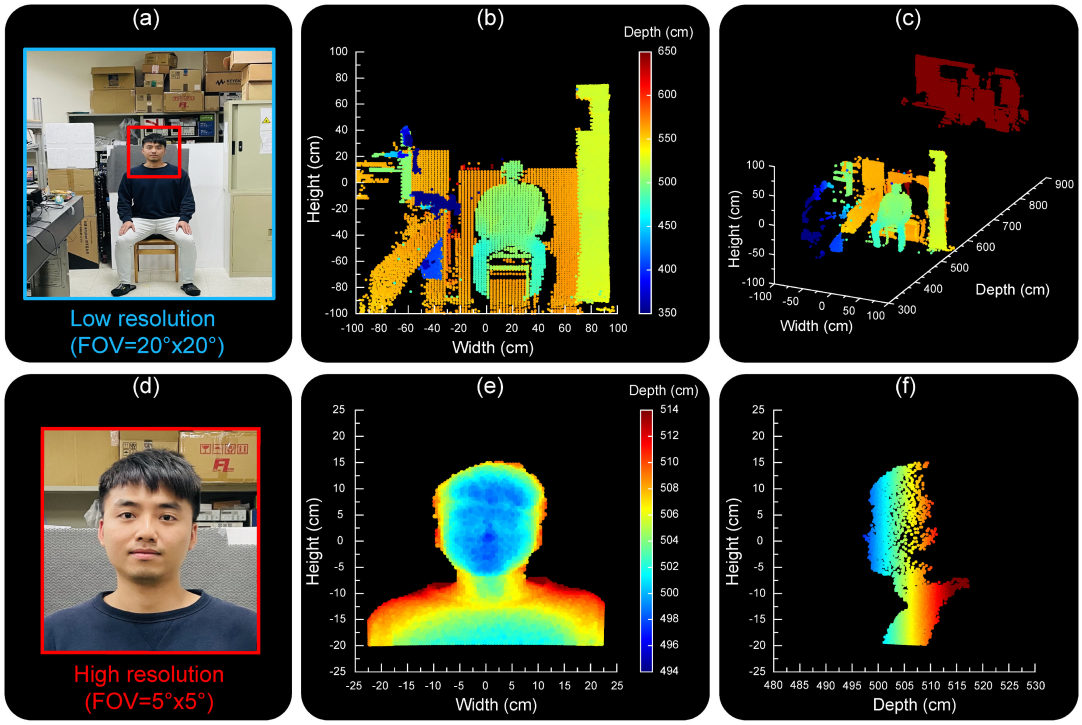

Fig. 7. (a) Photograph of a person seating in the laboratory environment and the (b) Front and (c) Bird's-eye views of its 3D rendering obtained using the acquired point cloud. (d) Photograph zoomed in on the face, the (e) Front, and (f) Side views of its 3D rendering obtained using the acquired point cloud. The large-FOV/low-resolution (blue box) and small-FOV/high-resolution (red box) images are scanned simultaneously. The FOVs, image resolutions, and angular resolutions are 20 × 20 degrees, 128 × 128 pixels, and 0.16 × 0.16 degrees for the low-resolution scan and 5 × 5 degrees, 128 × 128 pixels, and 0.04 × 0.04 degrees for the high-resolution scan, respectively. The person is seated approximately 5 m away from the lidar. The color in the 3D images depicts the depth.

VII. Demonstration of Multi-Channel Imaging with FOV Overlapped Scenes

To avoid interference, a conventional multi-channel pulsed lidar must either limit the FOV of each adjacent channel, emit the pulses of each channel at different times outside other's detection windows, or scan each channel with a particular pattern without overlapping each other on the same spot at the same time. By contrast, with a low correlation between each channel, the MIMO chaos lidar can scan a scene with channels overlapping each other but without interference.

In the demonstration presented in Fig. 7, we scanned a scene with two channels from the MIMO chaos lidar with overlapped FOVs. By scanning the two channels simultaneously, 3D images with large-FOV/low-resolution and small-FOV/high-resolution are obtained at the same time.

Figs. 7(a)–7(c) depict a photograph of a person seated 5 meters away from the lidar in a laboratory environment and the front and bird's-eye views of its 3D rendering obtained using the acquired point clouds. In the large FOV scan within the blue box, the FOV is 20 × 20 degrees, the image resolution is 128 × 128 pixels, and the angular resolution is 0.16 degrees both horizontally and vertically. To have such a large FOV, in this channel a quadrant APD (Idealphotonics QPD-1000) was used in the transceiver module to increase the detection area [29]. As can be seen, the posture of the person, the iron cabinet on the right, the optical table on the left, the cardboard, and the boxes behind are all clearly depicted.

By scanning simultaneously inside the red box shown in Fig. 7(a), the point clouds with a smaller FOV but higher resolution focus on the person's face are obtained. Figs. 7(d)–7(f) depict a photograph zoomed in on the face and the front and side views of its 3D rendering obtained using the acquired point clouds. In this small FOV scan, the FOV is 5 × 5 degrees, the image resolution is still 128 × 128 pixels, and the angular resolution is therefore increased by 4 times to 0.04 degrees both horizontally and vertically. Despite its low reflectivity and scattered nature, 3D images of the face with details in the orbits, nose, ears, and lips were obtained.

VIII. Conclusion

In summary, we developed a 3D MIMO pulsed chaos lidar based on time-division multiplexing. By time-gating chaos waveform in sequence at different times, chaos-modulated pulses uncorrelated to each other can be generated when the relative channel delay time τ_{ch} exceeds the pulsewidth *PW*. By using these pulses as the input pulse of each channel, interference among different channels can be mitigated. The PSL_{std}, precision, and detection probability under different relative jamming strengths and overlapped ratios were studied to quantify the anti-interference and anti-jamming capability. To consider both the detection probability and the occurrence probability for the jamming pulse to actually overlap with the signal pulse, the overall detection probabilities of the chaos lidar and TDC-based pulsed lidar were analyzed and compared. For relative jamming

strengths up to 11 dB, the overall detection probability of the chaos lidar can still be maintained above 98%.

For the first time, we demonstrated 3D imaging using MIMO chaos lidar under the influence of interference and malicious jamming. Moreover, by simultaneously scanning 2 different channels with overlapped FOVs, 3D images with large-FOV/low-resolution and small-FOV/high-resolution were obtained at the same time. From a system point of view, the detection throughput (pixel rate) was also doubled when the two channels are operated simultaneously. While we only show the results with 2 channels, MIMO chaos lidar with more channels can be easily realized. Moreover, we also studied an alternative scheme based on wavelength-division multiplexing which will be reported separately.

REFERENCES

[1] B. Schwarz, "Mapping the world in 3D," *Nature Photon.*, vol. 4, pp. 429–430, 2010.

[2] F. Moosmann and C. Stiller, "Velodyne SLAM," in *Proc. IEEE Intell. Veh. Symp.*, 2011, pp. 393–398.

[3] Q. Li, L. Chen, M. Li, S. L. Shaw, and A. Nüchter, "A sensor-fusion drivable-region and lane-detection system for autonomous vehicle navigation in challenging road scenarios," *IEEE Trans. Veh. Technol.*, vol. 63, no. 2, pp. 540–555, Feb. 2014.

[4] J. McCormack, J. Prine, B. Trowbridge, A. C. Rodriguez, and R. Integlia, "2D LIDAR as a distributed interaction tool for virtual and augmented reality video games," in *Proc. IEEE Games Entertainment Media Conf.*, 2015, pp. 1–5.

[5] M. C. Amann, T. M. Bosch, M. Lescure, R. A. Myllylae, and M. Rioux, "Laser ranging: A critical review of unusual techniques for distance measurement," *Opt. Eng.*, vol. 40, no. 1, pp. 10–19, 2001.

[6] J. D. Spinhirne, "Micro pulse lidar," *IEEE Trans. Geosci. Remote Sens.*, vol. 31, no. 1, pp. 48–55, Jan. 1993.

[7] G. Kim, J. Eom, and Y. Park, "Investigation on the occurrence of mutual interference between pulsed terrestrial LIDAR scanners," in *Proc. IEEE Intell. Veh. Symp.*, 2015, pp. 437–442.

[8] X. Ai, R. Nock, J. G. Rarity, and N. Dahnoun, "High-resolution random-modulation cw lidar," *Appl. Opt.*, vol. 50, no. 22, pp. 4478–4488, 2011.

[9] Z. Yang, C. Li, M. Yu, F. Chen, and T. Wu, "Compact 405-nm random-modulation continuous wave lidar for standoff biological warfare detection," *J. Appl. Remote Sens.*, vol. 9, no. 1, pp. 1–14, 2015.

[10] R. Matthey and V. Mitev, "Pseudo-random noise-continuous-wave laser radar for surface and cloud measurements," *Opt. Lasers Eng.*, vol. 43, no. 3, pp. 557–571, 2005.

[11] F. Y. Lin and J. M. Liu, "Chaotic lidar," *IEEE J. Sel. Topics Quantum Electron.*, vol. 10, no. 5, pp. 991–997, Sep.-Oct. 2004.

[12] W. T. Wu, Y. H. Liao, and F. Y. Lin, "Noise suppressions in synchronized chaos lidars," *Opt. Exp.*, vol. 18, no. 25, pp. 26155–26162, 2010.

[13] C. H. Cheng, Y. C. Chen, and F. Y. Lin, "Generation of uncorrelated multichannel chaos by electrical heterodyning for multiple-input-multiple-output chaos radar application," *IEEE Photon. J.*, vol. 8, no. 1, Feb. 2016, Art no. 7800209.

[14] F. Y. Lin and J. M. Liu, "Chaotic radar using nonlinear laser dynamics," *IEEE J. Quantum Electron.*, vol. 40, no. 6, pp. 815–820, Jun. 2004.

[15] F. Y. Lin, Y. K. Chao, and T. C. Wu, "Effective bandwidths of broadband chaotic signals," *IEEE J. Quantum Electron.*, vol. 48, no. 8, pp. 1010–1014, Aug. 2012.

[16] J. Mork, B. Tromborg, and J. Mark, "Chaos in semiconductor lasers with optical feedback: Theory and experiment," *IEEE J. Quantum Electron.*, vol. 28, no. 1, pp. 93–108, Jan. 1992.

[17] Y. H. Liao and F. Y. Lin, "Dynamical characteristics and their applications of semiconductor lasers subject to both optical injection and optical feedback," *Opt. Exp.*, vol. 21, no. 20, pp. 23568–23578, 2013.

[18] A. Uchida, T. Heil, Y. Liu, P. Davis, and T. Aida, "High-frequency broadband signal generation using a semiconductor laser with a chaotic optical injection," *IEEE J. Quantum Electron.*, vol. 39, no. 11, pp. 1462–1467, Nov. 2003.

[19] C. H. Cheng, Y. C. Chen, and F. Y. Lin, "Chaos time delay signature suppression and bandwidth enhancement by electrical heterodyning," *Opt. Exp.*, vol. 23, no. 3, pp. 2308–2319, 2015.

[20] T. Zhao, B. J. Wang, Y. C. Wang, and X. M. Chang, "Free space ranging utilizing chaotic light," *Math. Problems Eng.*, vol. 2013, pp. 1024–1230, 2013.

[21] R. Agishev, B. Gross, F. Moshary, A. Gilerson, and S. Ahmed, "Range-resolved pulsed and CWFM lidars: Potential capabilities comparison," *Appl. Phys. B*, vol. 85, pp. 149–162, 2006.

[22] M. U. Piracha *et al.*, "Range resolved lidar for long distance ranging with sub-millimeter resolution," *Opt. Exp.*, vol. 18, no. 7, pp. 7184–7189, 2010.

[23] *International Electrotechnical Commission (IEC)*, "Safety of Laser Products. Part 1: Equipment Classification, Requirements and User's Guide" Standard IEC 60825-1:2001, International Electrotechnical Commission, 2001, pp. 20–40.

[24] C. H. Cheng, C. Y. Chen, J. D. Chen, D. K. Pan, K. T. Ting, and F. Y. Lin, "3D pulsed chaos lidar system," *Opt. Exp.*, vol. 26, no. 9, pp. 12230–12241, 2018.

[25] H. L. Tsay, C. Y. Wang, J. D. Chen, and F. Y. Lin, "Generations of chaos-modulated pulses based on a gain-switched semiconductor laser subject to delay-synchronized optical feedback for pulsed chaos lidar applications," *Opt. Exp.*, vol. 28, no. 16, pp. 24037–24046, 2020.

[26] C. Y. Chen, C. H. Cheng, D. K. Pan, and F. Y. Lin, "Experimental generation and analysis of chaos-modulated pulses for pulsed chaos lidar applications based on gain-switched semiconductor lasers subject to optical feedback," *Opt. Exp.*, vol. 26, no. 16, pp. 20851–20860, 2018.

[27] K. T. Ting and F. Y. Lin, "Generation of random on-off modulation pulses by optically injecting a gain-switched fabry-pérot semiconductor laser with a dual-mode injection for random-modulation pulsed lidar applications," *Opt. Exp.*, vol. 26, no. 19, pp. 24294–24306, 2018.

[28] J. D. Chen *et al.*, "3D chaos lidar system with a pulsed master oscillator power amplifier scheme," *Opt. Exp.*, vol. 29, no. 17, pp. 27871–27881, 2021.

[29] H. L. Ho *et al.*, "High-speed 3D imaging using a chaos lidar system," *Eur. Phys. J. Special Topics*, pp. 1–7, Jan. 2022, doi: https://doi.org/10.1140/epjs/s11734-021-00410-8.

[30] R. Halterman and M. Bruch, "Velodyne HDL-64E lidar for unmanned surface vehicle obstacle detection," in *Unmanned Syst. Technol. XII*, vol. 7692. International Society for Optics and Photonics, 2010, Art. no. 76920D.

[31] P. F. McManamon, "Design considerations for an auto LiDAR," in *Proc. Ind. Opt. Devices Syst.*, vol. 11125. International Society for Optics and Photonics, 2019, Art. no. 111250G.

[32] J. G. Wu *et al.*, "Time delay signature concealment of optical feedback induced chaos in an external cavity semiconductor laser," *Opt. Exp.*, vol. 18, no. 7, pp. 6661–6666, 2010.

[33] D. Wang *et al.*, "Time delay signature elimination of chaos in a semiconductor laser by dispersive feedback from a chirped FBG," *Opt. Exp.*, vol. 25, no. 10, pp. 10911–10924, 2017.

[34] G. Wahba, "Spline interpolation and smoothing on the sphere," *SIAM J. Sci. Stat. Comput.*, vol. 2, no. 1, pp. 5–16, 1981.

[35] L. Svilainis, K. Lukoseviciute, V. Dumbrava, and A. Chaziachmetovas, "Subsample interpolation bias error in time of flight estimation by direct correlation in digital domain," *Meas.*, vol. 46, no. 10, pp. 3950–3958, 2013.

[36] L. Svilainis, "Review on time delay estimate subsample interpolation in frequency domain," *IEEE Trans. Ultrason., Ferroelectr., Freq. Control*, vol. 66, no. 11, pp. 1691–1698, Nov. 2019.

Jun-Da Chen received the B.S. degree from the Department of Joint Science Program (Optics and Photonics), National Central University, Taoyuan, Taiwan, in 2014, and the M.S. degree from the Institute of Photonics Technologies, National Tsing Hua University, Hsinchu, Taiwan, in 2017. He is currently working toward the Ph.D. degree with the Institute of Photonics Technologies, National Tsing Hua University, Hsinchu, Taiwan. His research interests include nonlinear dynamics of semiconductor lasers, interpolation algorithms, pulsed MOPA scheme, and MIMO chaos lidar system.

Kuan-Wei Wu received the B.S. degree from the Department of Photonics Engineering, Yuan Ze University, Taoyuan, Taiwan, in 2018, and the M.S. degree from the Institute of Photonics Technologies, National Tsing Hua University, Hsinchu, Taiwan, 2021. His research interests include the nonlinear dynamics of semiconductor lasers and MIMO chaos lidar systems.

Hsin-Lin Ho received the B.S. degree from the Department of Photonics, National Sun Yat-sen University, Kaohsiung, Taiwan, in 2017, and the M.S. degree from the Institute of Photonics Technologies, National Tsing Hua University, Hsinchu, Taiwan, in 2020. He is currently a Research Assistant with the Institute of Photonics Technologies, National Tsing Hua University, Hsinchu, Taiwan. His research interests include nonlinear dynamics of semiconductor lasers, pulsed MOPA scheme, and MIMO chaos lidar system.

Cheng-Ting Lee received the B.S. degree from the Department of Photonics, Feng Chia University, Taichung, Taiwan, in 2019. He is currently working toward the Ph.D. degree with the Institute of Photonics Technologies, National Tsing Hua University, Hsinchu, Taiwan. His research interests include nonlinear dynamics of semiconductor lasers, TIA design, and MIMO chaos lidar system.

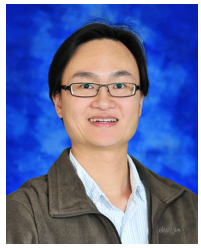

Fan-Yi Lin (Member, IEEE) received the B.S. degree in electrophysics from National Chiao Tung University, Hsinchu, Taiwan, in 1997, and the M.S. and Ph.D. degrees in electrical engineering from the University of California, Los Angeles, CA, USA, in 2001 and 2004, respectively. He joined the Department of Electrical Engineering and Institute of Photonics Technologies, National Tsing Hua University, Hsinchu, Taiwan, in 2004 and became a Full Professor in 2015. Since 2018, he has been appointed as the Director of the Institute of Photonics Technologies, National Tsing Hua University. His research interests include laser dynamics, lidar and radar, chaos, and photonic microwave generation.